ChemPubSoc Europe

DOI: 10.1002/open.201900091

Open Access ChemistryOPEN Full Papers

Synthesis and Characterization of Ru-Loaded Anodized Aluminum Oxide for Hydrogenation Catalysis

Annelies Vandekerkhove,[a] Leila Negahdar,[b] Daan Glas,[a] Ivo Stassen,[a] Serguei Matveev,[b] Johannes D. Meeldijk,[b] Florian Meirer,[b] Dirk E. De Vos,*[a] and Bert M. Weckhuysen*[b]

Anodized aluminum oxides (AAOs) are synthesized and used as catalyst support in combination with Ru as metal in hydrogenation catalysis. SEM and TEM analysis of the as-synthesized AAOs reveal uniform, ordered nanotubes with pore diameters of 18 nm, which are further characterized with Kr physisorption, XRD and FTIR spectroscopy. After impregnation of the AAOs with Ru, the presence of Ru nanoparticles inside the tubular pores is evidenced clearly for the first time via HAADF-STEM-EDX. The Ru–AAOs have been tested for catalytic activity, which showed high conversion and selectivity for the hydrogenation of toluene and butanal.

1. Introduction

One of the most important advantages of heterogeneous catalysis over its homogeneous counterparts is that the catalyst can be easily removed from the reaction mixture since the catalyst is in a different phase compared to the reactants. Heterogeneous catalysts are, however, very often used as a powder, implying the need for an additional centrifugation or filtration step to separate the catalyst from the reaction mixture. Therefore, shaping catalysts as e.g. monoliths, pellets and extrudates is more practical especially in large-scale industrial applications.[1] A second important characteristic of many heterogeneous catalysts are the pores. Micro-, meso- and macro-porous catalysts with pore sizes ranging from <2 nm, 2–50 nm and >50 nm respectively can be identified. Microporous catalysts, e.g. zeolites, have numerous applications but often suffer from diffusional limitations.[2] Alternatively mesoporous catalysts, such as MCM and SBA type materials, can be applied.[3]

AAOs are a type of material that combine both above-mentioned advantages. Instead of a powder, they are designed as platelets that can be immersed into and easily taken out of reaction mixtures. Moreover, the uniform, tubular pores are in the mesoporous range, allowing easy diffusion of reactants and products. Therefore, it would be very promising to use AAOs as catalyst supports. These advantages originate from the specific electrochemical synthesis procedure of AAOs, comprising four steps (Scheme 1).[4,5] Aluminum surfaces, which are used as starting material, are electropolished in the first step to remove all impurities from the surface, rendering a clean aluminum surface. During the first anodization, irregular pores are formed while aluminum is oxidized to Al_2O_3. These pores are chemically etched in the third step and lastly, a second anodization leads to the formation of highly ordered, uniform, tubular pores.

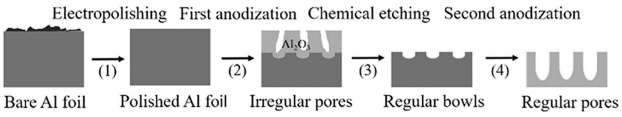

Scheme 1. Schematic representation of the electrochemical anodized aluminum oxides (AAO) synthesis procedure.[4,5]

The AAOs are often applied in fields different from catalysis, such as sensing, biocompatibilization and as templates for other nanostructures, for instance nanotubes, -wires, -rods.[6–8] However, only few studies considered the catalytic activity of the AAOs.[9–14] Different transition metals (e.g. Pd, Pt, Cu and Co) were tested for their activity for instance in hydrogenation and steam reforming reactions. The presence of the active metal inside the pores is always presumed, nevertheless, to our knowledge, never unambiguously evidenced. In this work, AAOs are synthesized and impregnated with Ru and a clear proof of the presence of Ru nanoparticles inside the pores is provided with HAADF-STEM-EDX. The resulting Ru–AAOs are investigated for their catalytic activity in the hydrogenation of toluene and butanal as model reactions for aromatics and carbonyl reductions.

[a] A. Vandekerkhove, Dr. D. Glas, Dr. I. Stassen, Prof. Dr. D. E. De Vos
Department of Microbial and Molecular Systems, Centre for Surface Chemistry and Catalysis
KU Leuven
Celestijnenlaan 200F, P.O. 2461, 3001 Heverlee, Belgium
E-mail: dirk.devos@kuleuven.be

[b] Dr. L. Negahdar, Dr. S. Matveev, Dr. J. D. Meeldijk, Prof. Dr. F. Meirer, Prof. Dr. B. M. Weckhuysen
Inorganic Chemistry and Catalysis, Debye Institute for Nanomaterials Science
Utrecht University
Universiteitsweg 99, 3584 CG Utrecht, The Netherlands
E-mail: b.m.weckhuysen@uu.nl

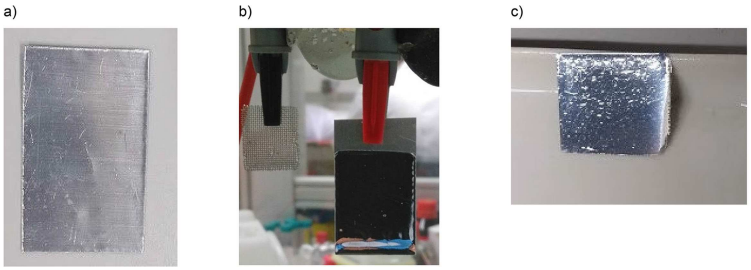

Figure 1. Pictures of a) aluminum platelet (2×3.3 cm^2) before anodization; b) platelet (2×3.3 cm^2) during anodization (right) and Pt cathode (left); c) AAO (2×2.4 cm^2) after anodization and drying.

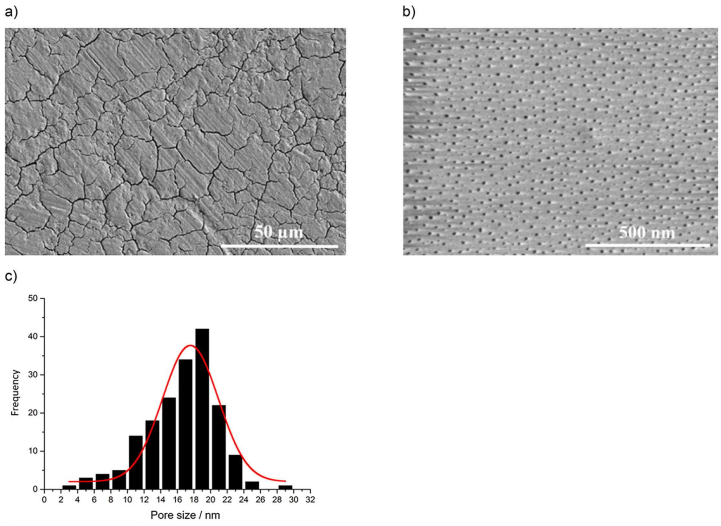

Figure 2. a) Top-view SEM micrograph of an as-synthesized AAO at 21 V; b) Top-view SEM micrograph of an as-synthesized AAO at 19 V; c) pore size distribution of an as-synthesized AAO.

2. Results and Discussion

2.1. Synthesis and Characterization of AAOs

Anodized aluminum oxides (AAOs) with highly regular pores are produced during the controlled anodization of aluminum platelets. Pictures of the platelets before, during and after synthesis are shown in Figure 1. It seems crucial to control the anodization voltage: applying 21 V leads to a cracked, rough surface compared to platelets prepared at 19 V (Figure 2, a and b). Moreover, no pores are visible from the outer surface, which would suggest that during catalytic reactions, the reactants are not capable to diffuse through the pores, leading to a very low catalytic activity. The platelet synthesized at 19 V exhibits circular pores evenly covering the entire surface (Figure 2, b). The pore size distribution is rather narrow, and the average pore diameter is determined to be 17 ± 4 nm, by fitting a Gaussian curve onto the pore size distribution (Figure 2, c). The side-views of the as-synthesized AAO, presented by the TEM micrographs, display highly ordered, tubular pores, extending over a long range (i.e. surfaces of several square millimeters) and open at the surface (Figure 3, a). On a smaller scale, the uniform pore size can be clearly observed (Figure 3, b). Both Figure 2 and Figure 3 clearly prove that the anodization

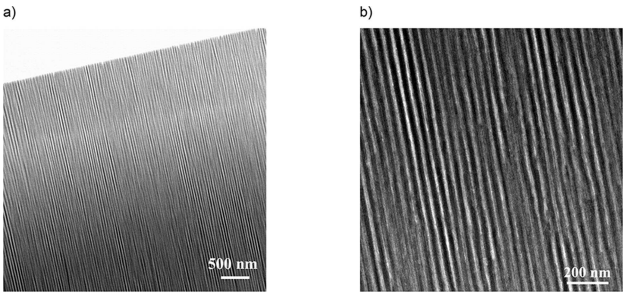

Figure 3. Side-view TEM micrographs of an as-synthesized AAO, a) long range order; b) smaller scale.

procedure developed in this work, produces AAOs with the desired, highly ordered, cylindrical mesopores. Upon investigating the complete cross-section, three zones can be identified (Figure 4). The two outer zones consist of alumina and this is the zone where the pores are located, with heights of around 95 ± 5 µm. In contrast, the middle part is unreacted aluminum with a height of 48 ± 5 µm; it does not contain any porosity. The total thickness of the plate after anodization consequently is 230 ± 15 µm.

The porosity and BET surface area of the as-synthesized AAO were determined *via* Kr physisorption (Figure 5) since the

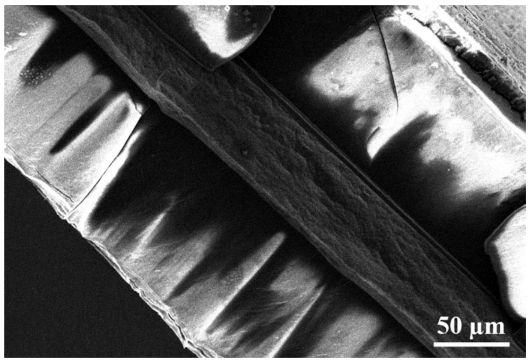

Figure 4. Cross-sectional SEM micrograph of an as-synthesized AAO.

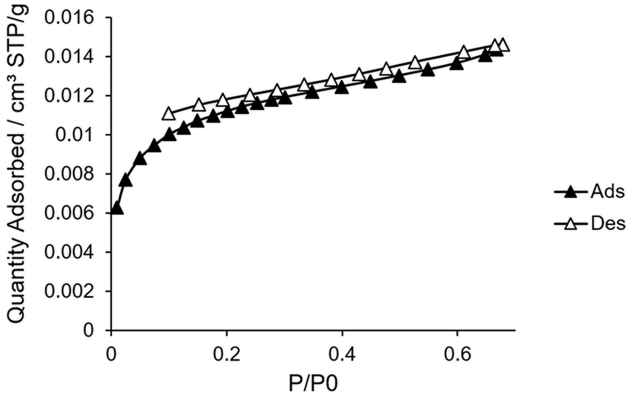

Figure 5. Kr physisorption isotherm of an as-synthesized AAO. (▲ adsorption isotherm; Δ desorption isotherm).

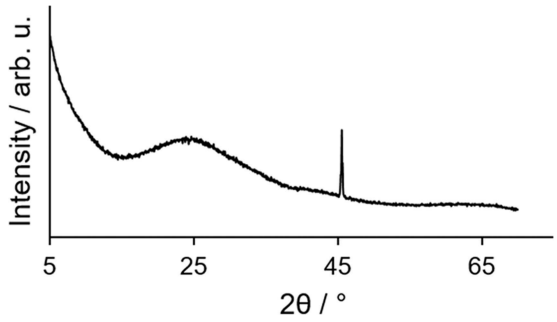

Figure 6. XRD diffractogram of an as-synthesized AAO.

porosity on mass basis is very low and Kr physisorption is more sensitive compared to N_2 physisorption.[15] The isotherm is similar to the onset of a type IV isotherm with a constant positive slope in the range of 0.2–0.68 P/P_0, indicating multilayer adsorption in large pores. The BET specific surface area is determined to be 1.21 m^2/g, which seems rather low. However, when comparing the specific surface of the plate (with a weight of typically 0.3 g, and dimensions $2\times3.3\ cm^2$) with the BET specific surface area, a 275-fold increase of the surface is achieved (equations (1) and (2)).

$$Outer\ surface: 2^{*}area\ AAO = 2^{*}2\ cm^{*}3.3\ cm = 13.2\ cm^2 \quad (1)$$

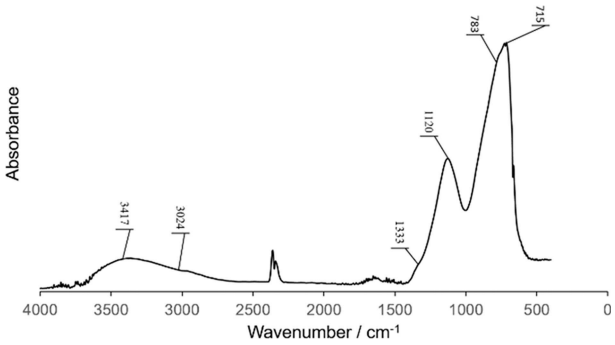

Figure 7. FTIR spectrum of an as-synthesized AAO.

$$Specific\ outer\ surface\ area: \frac{outer\ surface\ area}{weight\ of\ AAO} = \frac{13.2\ cm^2}{0.3\ g} = 4.4^{*}10^{-3}\frac{m^2}{g} \quad (2)$$

Although the AAOs in this work were not subject to calcination or hot water treatment, we attempted to determine the alumina phase here via XRD and FTIR spectroscopy. From the XRD diffractogram, mainly amorphous alumina can be observed (Figure 6). Only one peak at 45.6° is present, which can be related to metallic aluminum, most probably originating from the aluminum sample holder.

The FTIR spectrum reveals several bands that can be attributed to different vibration modes (Figure 7). The bands at 3417 and 3024 cm^{-1} represent OH-stretching. At 1333 and 1120 cm^{-1}, Al–OH stretching and bending of tetrahedral aluminum is observed, respectively, while Al–O stretching of octahedral aluminum is assigned to the bands at 783 and 715 cm^{-1}. Since hydroxyl species and tetrahedral aluminum are present, the alpha-alumina phase is excluded; nevertheless, no clear phase can represent the AAOs produced here. Although an additional calcination step would most likely lead to the formation of a single alumina phase, the highly ordered pore structure of the AAO could be damaged. In this work, it is important to retain the pore structure, as Ru will be impregnated inside the pores and the Ru–AAO will be used as catalyst in hydrogenation reactions.

2.2. Synthesis and Characterization of Ru-Loaded AAOs

Although incipient wetness impregnation is often the method of choice for the preparation of heterogeneous catalysts, this method is not suitable for the AAOs synthesized in this work, due to the low pore volume of 3 µl per AAO platelet. Consequently, a Ru-precursor solution is transferred to a watch glass in which the AAO is immersed immediately after drying. Both water and ethanol are tested as solvent, resulting in differing impregnation behavior, largely because of the different surface tensions in the wetting/filling of the pores. After use of an aqueous Ru-precursor solution, HAADF-STEM(-EDX) reveals that Ru is present only on the outer surface of the AAO

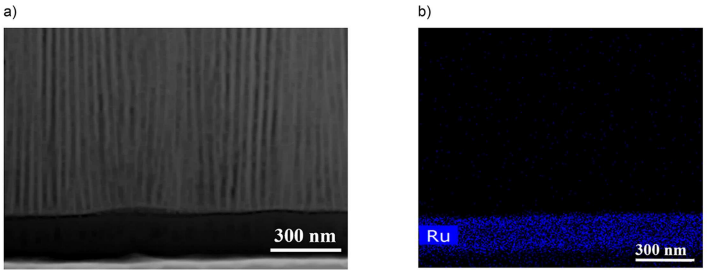

Figure 8. Elemental mapping of the internal tubes of AAO catalyst impregnated with aqueous Ru-precursor solution. a) HAADF-STEM micrograph; b) HAADF-STEM-EDX elemental mapping of Ru.

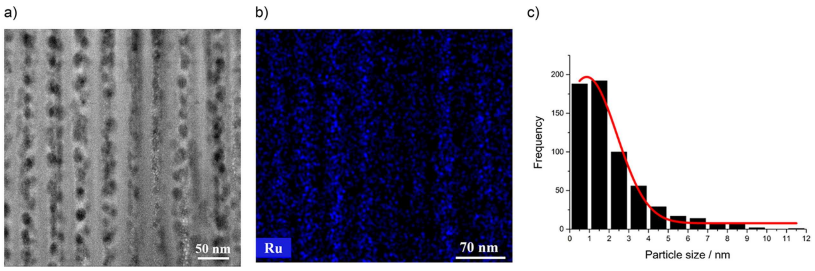

Figure 9. Elemental mapping of the internal tubes of AAO catalyst impregnated with ethanolic Ru-precursor solution. a) HAADF-STEM micrograph; b) HAADF-STEM-EDX elemental mapping of Ru; c) particle size distribution of the Ru particles in the AAO pores.

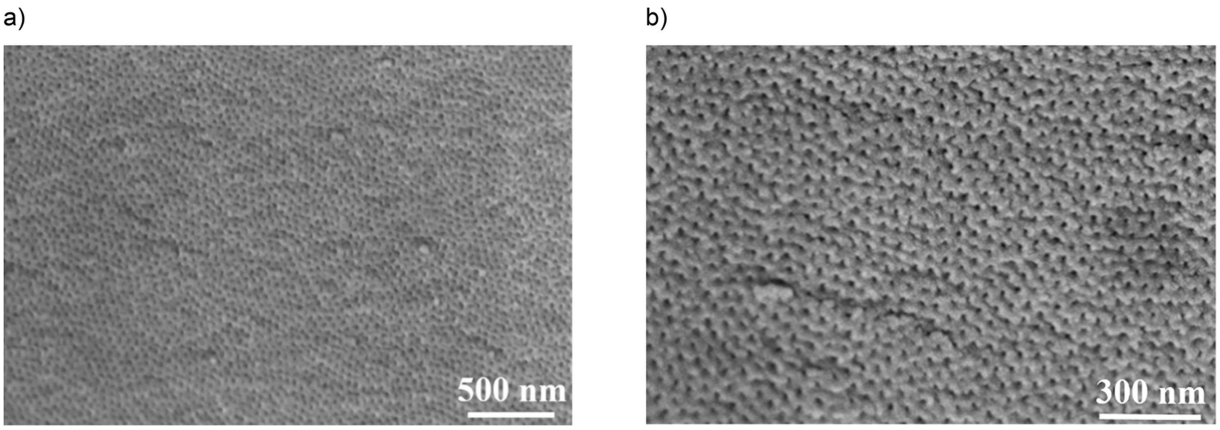

Figure 10. SEM micrographs of AAO catalyst impregnated with ethanolic Ru-precursor solution. a) pores visible on large scale; b) smaller scale.

in a thick layer and that it does not penetrate into the pores of the AAO (Figure 8, a and b). The high contact angle of water with anodized aluminum oxide (around 62–73°) results in a poor wettability of the AAO surface and accordingly, Ru is not at all deposited inside the pores, which has indeed been described in the literature.[16]

Ethanol is a more suitable solvent for Ru impregnation on AAOs. It has a lower contact angle with the AAO platelet and the Ru-precursor solution can indeed wet the surface. Therefore, the solution can enter the pores and Ru can be deposited as Ru nanoparticles inside the tubes. This is clearly demonstrated using HAADF-STEM(-EDX) (Figure 9, a and b). To the best of our knowledge, the presence of the active metal in the AAO pores is clearly evidenced for the first time by a combination of HAADF-STEM and elemental mapping via EDX; former studies mostly rely only on (S)TEM characterization without elemental mapping of the catalyst; or they used XPS and XRD which give no spatial information on the location of the metal nanoparticles.[9–14,17] The Ru particles are rather small (mainly 1–3 nm), ensuring that the pores are not blocked with Ru (Figure 9, c). Also, the outer surface of the pores is not obstructed, as the pore mouths are still visible in the SEM micrographs (Figure 10, a and b). Consequently, diffusion of the substrate and product molecules in and out of the pores during hydrogenations is still guaranteed.

Table 1. Summary of the performances of Ru–AAO in the catalytic hydrogenation of levulinic acid, toluene and butanal.

Entry	Substrate	Product	Time (h)	Conversion (%)	Selectivity (%)
1[a]	Levulinic acid	γ-Valerolactone	6	98	93
2[a]	Levulinic acid	γ-Valerolactone	20	>99	94
3[b]	Toluene	Methylcyclohexane	6	43	95
4[b]	Toluene	Methylcyclohexane	16	73	95
5[c]	Butanal	Butanol	2	63	>99
6[c]	Butanal	Butanol	6	>99	>99

Conditions: [a]Levulinic acid (0.5 M), Ru–AAO (Ru/levulinic acid = 1.5 mol%), water (10 ml), H_2 (50 bar), 150 °C. [b]Toluene (2.1 mM), Ru–AAO (Ru/toluene = 3.5 mol%), methanol (9 ml), H_2 (30 bar), 40 °C. [c]Butanal (0.5 M), Ru–AAO (Ru/butanal = 1.5 mol%), water (10 ml), H_2 (50 bar), 90 °C.

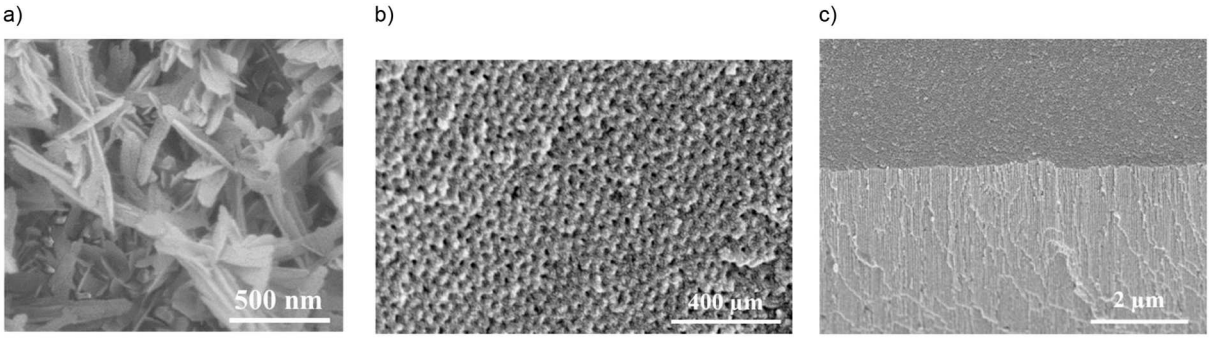

Figure 11. SEM micrographs of a) Ru–AAO surface after hydrogenation of levulinic acid; b) Ru–AAO surface after hydrogenation of butanal; c) side-view of Ru–AAO after hydrogenation of butanal.

2.3. Catalysis with Ru–AAOs

To examine the catalytic activity of the developed Ru–AAOs, hydrogenation reactions are performed. Levulinic acid is a platform chemical from lignocellulosic biomass and its hydrogenation product, γ-valerolactone is a valuable chemical with applications as green solvent, fuel and intermediate in synthesis of several value-added chemicals.[18] The hydrogenation of levulinic acid leads to excellent catalytic activity and selectivity after 6 h and 20 h (Table 1, entry 1,2). The conversions are above 98% and the cyclic hydrogenation product γ-valerolactone is obtained at >93% selectivity. Nevertheless, the catalyst seems unstable under the reaction conditions as SEM micrographs exhibit the formation of crystals on the AAO surface (Figure 11, a).

Indeed, the reduction proceeds in acidic water, leading to dissolution of the Al_2O_3-phase and its recrystallization on the AAO surface.

In order to avoid Al_2O_3 dissolution and recrystallization, toluene and butanal are reduced, as model substrates of aromatic and aldehyde compounds respectively. The catalyst activity for toluene hydrogenation is lower than for levulinic acid, showing 73% conversion after 16 h (Table 1, entry 3,4). The selectivity to methylcyclohexane is very high (95%) and 3-methylcyclohexene is a minor byproduct. On the other hand, butanal is reduced more easily with conversion and selectivity above 99% after 6 h (Table 1, entry 5). From elemental analysis of the reaction mixture after butanal hydrogenation, the Ru leaching is determined to be only 0.06%, which is very limited. Also, the Ru–AAO pore structure remains intact after the hydrogenation, which can be seen both from the surface (Figure 11, b) and from the nanotubes in the side-view (Figure 11, c).

To verify whether the reaction proceeds under diffusional control, the Thiele modulus is calculated according to Equation 3, with k the rate constant, L the characteristic length, D the diffusion coefficient:

$$\phi = \sqrt{\frac{k^* L^2}{D}} \tag{3}$$

Rate constants can be derived from the initial rates, both for toluene hydrogenation ($2.0\ 10^{-5}\ s^{-1}$) and for butanal hydrogenation ($8.8\ 10^{-5}\ s^{-1}$), according to the reactions performed in the conditions in Table 1. The characteristic length is derived from the channels' depth, which is ≤95 µm. While the value of the diffusion coefficients in the porous support could depend on the experimental technique, a safe (minimal) estimate can be found in a recent study by Gläser, for toluene diffusion in porous glass with a pore diameter of 10 nm.[19] This resulted in values of $1.3\ 10^{-9}\ m^2\ s^{-1}$ (at 313 K) and $3\ 10^{-9}\ m^2 s^{-1}$ (at 363 K). With these values, the Thiele modulus is calculated according to Equation 3. Values obtained are $\varphi = 0.011$ (for toluene hydrogenation) and $\varphi = 0.016$ (for butanal hydrogenation). Both values are <1, from which it can be concluded that the hydrogenation reactions on the AAO supports do not proceed under diffusional control.

3. Conclusions

Anodized aluminum oxides (AAOs) with uniform, tubular pores were synthesized according to a four-step electrochemical synthesis procedure. The AAOs are used as catalyst supports and are impregnated with Ru to create Ru-based hydrogenation catalyst materials. Using SEM and TEM analysis, AAOs were characterized and the presence of uniform, ordered nanopores with pore diameter of 17 ± 4 nm was confirmed. To the best of our knowledge, the presence of Ru nanoparticles inside the tubular pores is evidenced for the first time *via* HAADF-STEM-EDX. The Ru–AAO catalysts are employed in hydrogenation reactions of toluene and butanal as model compounds of aromatics and aldehydes. High catalytic activity is obtained and no diffusional limitation is observed. After the reaction, the pores of the AAOs remain preserved. It can thus be concluded that the AAOs synthesized in this work exhibit uniform, ordered nanopores with high catalytic activity, opening up the possibility to make catalyst materials for other reactions.

Experimental Section

Materials and Catalyst Synthesis

All chemicals were purchased and used without further purification: aluminum foil (Alfa Aesar, 0.25 mm thick, annealed, 99.99% (metals basis)), perchloric acid ($HClO_4$, Acros Organics, for analysis, ca. 70% solution in water), ethanol (Fischer Chemical, absolute), sulfuric acid (Fischer Chemical, S.G. 1.83 (>95%)), nitric acid (Sigma Aldrich, puriss. p.a., reag. ISO, reag. Ph. Eur., for determinations with dithizone, ≥65%), acetic acid (VWR Chemicals, 100%), orthophosphoric acid (VWR Chemicals, 85%, ACS, Reag. Ph. Eur), ruthenium (III) chloride hydrate (Alfa Aesar, Premion 99.99% (metals basis)), levulinic acid (Acros Organics, 98+%), toluene (Acros Organics, 99.8+%, for analysis), methanol (VWR Chemicals), butanal (Acros Organics, 99%), deuterium oxide (Sigma-Aldrich, 99.9 atom% D) and n-nonane (Acros Organics, 99% pure).

The synthesis procedure for the AAO platelets used in this study was optimized starting from procedures described in the literature.[20–23] A high purity aluminum sheet (99.99%), with a thickness of 0.25 mm is first cut into platelets of 2×3.3 cm^2. The platelet is degreased with acetone and undergoes a four-step anodization procedure with platinum gauze as the cathode while the aluminum platelet is the anode. During the electropolishing step, the platelet is immersed in a 20 vol% $HClO_4$ in ethanol solution. Subsequently, a voltage of 12 V and a maximum current of 1 A are applied for 10 min at 10 °C. The first anodization step is carried out at 0 °C for 10 min in a 20 wt% H_2SO_4 solution at 19–21 V with 1 A as maximum current. Thirdly, the platelet is immersed in a 5 wt% HNO_3 (65 wt% in H_2O) – 5 wt% acetic acid – 75 wt% H_3PO_4 (85 wt% in H_2O) solution at 40 °C for 5 min during the chemical etching step. The last step is again an anodization step in the same solution and at the same voltage and current, at 0 °C for 7 h. After the anodization procedure, the AAO is stored in H_2O until it is dried at 100 °C for 15 min.

In a final step, Ru is deposited onto the AAOs via an impregnation method. $RuCl_3$ hydrate is dissolved in 5 ml H_2O or ethanol with Ru/substrate = 1.5 mol% and the solution is transferred to a watch glass. Immediately after drying the AAO, the platelet is immersed into the Ru precursor solution and the solvent is evaporated at room temperature. A prereduction of Ru–AAOs is performed at 150 °C and 50 bar H_2 for 24 h.

Catalyst Characterization

To calculate the BET specific surface area, Kr physisorption isotherms are measured on a Micromeritics 3Flex Surface Analyzer at 77 K. X-ray diffraction data were recorded on a Malvern PANalytical Empyrean diffractometer equipped with a PIXcel3D solid state detector using a Cu anode (Cu Ka1: 1.5406 Å; Cu Ka2: 1.5444 Å). Samples were placed on a programmable stage motorized in the x, y and z directions. Before each measurement, an iterative scheme was employed to optimize both sample height (z) and sample tilt (ω). Grazing incidence diffraction patterns were recorded at room temperature in reflection geometry (Bragg-Brentano, incident beam angle 0.2°) within a 5°–70° range using a step size of 0.053° and a counting time of 1000 s per step. On the incident beam side, a 1/16° fixed anti-scatter slit was used to limit the divergence of the beam. FTIR spectra are recorded on a Bruker Optics IFS 66 V/S spectrometer (128 scans, 4 cm^{-1} resolution, 500 ~ 4000 cm^{-1}) under vacuum. The surface morphology of the AAOs is measured on a SEM (FEI-Helios Nanolab G3UC) at an accelerating voltage of 10 kV. TEM micrographs are obtained on a FEI-Talos F200x; prior to the analysis, the surface of the AAO sample is coated with Pt to enhance the conductivity. The Ru content in the catalyst samples is analyzed by EDX (Oxford X–MaxN 150 SSD) attached to SEM.

Catalyst Testing

Hydrogenation reactions are performed in a 15 mL stainless steel autoclave. A Teflon ring is placed at the bottom of the reactor with a magnetic stirrer in the center of the ring. The Ru–AAO is placed on top of the ring, the solvent and substrate are added and the reactor is sealed. The magnetic stirrer ensures mixing throughout the whole reaction mixture. First, the autoclave is purged 3 times with N_2 and subsequently 3 times with H_2 and then, the reactor is pressurized with H_2 and the reaction temperature is applied. After the applied reaction time, the reactor is cooled down on ice and the catalyst platelet is removed. The reaction mixture is then analyzed by NMR or GC(-MS).

Reaction products are identified and quantified with ^{1}H-NMR for hydrogenations performed in H_2O. Samples for ^{1}H-NMR are prepared by adding 300 µl of reaction mixture to 300 µl of D_2O. The Bruker Ascend 400 MHz spectrometer is equipped with a BBO 5 mm atma probe. In order to suppress the water signal at 4.7 ppm, the following pulse program is used: p1 8 µs; plw1 15 W; plw9 $5.7 \cdot 10^{-5}$; o1P on the resonance signal of water, which is automatically determined and selected.

For reactions carried out in ethanol, gas chromatography coupled to a mass spectrometer (GC-MS) is used for product identification. An Agilent 6890 GC provided with an HP-5 ms column and coupled to a 5973 MSD mass spectrometer are used. Quantification of these reaction mixtures is done by GC analysis on a Shimadzu GC-2010 instrument with a 60 m CP SIL 5 CB column and an FID detector. Nonane is used as an internal standard.

ICP-OES analysis was used to determine the Ru content of the reaction mixture of butanal hydrogenation using a Varian 720-ES equipped with a double-pass glass cyclonic spray chamber, a Sea Spray concentric glass nebulizer and a high solids torch.

Acknowledgements

This work is financially supported by the CAPITA-WAVES: WAste bio-feedstocks hydro-Valorisation processES", 13CAPITA-13-6 Project. We would like to thank Carlos Marquez for his assistance with the ICP and additional SEM measurements.

Conflict of Interest

The authors declare no conflict of interest.

Keywords: anodized aluminum oxide · hydrogenation · Ru catalysts · butanal · toluene

[1] M. Campanati, G. Fornasari, A. Vaccari, *Catal. Today* **2003**, *77*, 299–314.
[2] S. Van Donk, A. H. Janssen, J. H. Bitter, K. P. De Jong, *Catal. Rev. Sci. Eng.* **2003**, *45*, 297–319.
[3] A. Sayari, *Chem. Mater.* **1996**, *8*, 1840–1852.
[4] M. H. Lee, N. Lim, D. J. Ruebusch, A. Jamshidi, R. Kapadia, H. Jang, M. Wu, G. Cho, A. Javey, *Nano Lett.* **2011**, *11*, 3425–3430.
[5] G. E. J. Poinern, N. Ali, D. Fawcett, *Materials (Basel).* **2011**, *4*, 487–526.
[6] A. M. Jani, D. Losic, N. H. Voelcker, *Prog. Mater. Sci.* **2013**, *58*, 636–704.
[7] T. Kumeria, A. Santos, D. Losic, *Sensors* **2014**, *14*, 11878–918.
[8] Q. Xu, G. Meng, F. Han, *Prog. Mater. Sci.* **2018**, *95*, 243–285.
[9] R. Hong, J. Feng, Y. He, D. Li, *Chem. Eng. Sci.* **2015**, *135*, 274–284.
[10] J. Karuppiah, E. Linga Reddy, Y. Mok, *Catalysts* **2016**, *6*, 154.
[11] E. Linga Reddy, J. Karuppiah, H. C. Lee, D. H. Kim, *J. Power Sources* **2014**, *268*, 88–95.
[12] Z. Rui, C. Chen, Y. Lu, H. Ji, *Chin. J. Chem. Eng.* **2014**, *22*, 882–887.
[13] B. R. Tzaneva, A. I. Naydenov, S. Z. Todorova, V. H. Videkov, V. S. Milusheva, P. K. Stefanov, *Electrochim. Acta* **2016**, *191*, 192–199.
[14] Q. Zhang, F. Fan, G. Xu, D. Ye, W. Wang, Z. Zhu, *Int. J. Hydrogen Energy* **2013**, *38*, 10305–10314.
[15] M. Thommes, K. A. Cychosz, *Adsorption* **2014**, *20*, 233–250.
[16] R. Redón, A. Vázquez-Olmos, M. E. Mata-Zamora, A. Ordóñez-Medrano, F. Rivera-Torres, J. M. Saniger, *Rev. Adv. Mater. Sci.* **2006**, *11*, 79–87.
[17] Q. Zhang, J. Xu, F. Fan, D. Sun, G. Xu, S. Zhang, Z. Zhu, *Fuel Process. Technol.* **2014**, *119*, 52–59.
[18] D. M. Alonso, S. G. Wettstein, J. A. Dumesic, *Green Chem.* **2013**, *15*, 584–595.
[19] M. Goepel, H. Kabir, C. Küster, E. Saraçi, P. Zeigermann, R. Valiullin, C. Chmelik, D. Enke, J. Kärger, R. Gläser, *Catal. Sci. Technol.* **2015**, *5*, 3137–3146.
[20] G. D. Sulka, W. J. Stepniowski, *Electrochim. Acta* **2009**, *54*, 3683–3691.
[21] G. D. Sulka, K. G. Parkoła, *Electrochim. Acta* **2007**, *52*, 1880–1888.
[22] L. Zaraska, G. D. Sulka, J. Szeremeta, M. Jaskuła, *Electrochim. Acta* **2010**, *55*, 4377–4386.
[23] L. Fernández-Romero, J. M. Montero-Moreno, E. Pellicer, F. Peiró, A. Cornet, J. R. Morante, M. Sarret, C. Müller, *Mater. Chem. Phys.* **2008**, *111*, 542–547.

Manuscript received: March 13, 2019